NbSe 2 Nanosheets/Nanorolls Obtained via Fast and Direct Aqueous Electrochemical Exfoliation for High-Capacity Lithium Storage

Daniel F Carrasco, Sergio García-Dalí, Silvia Villar-Rodil, José M Munuera, Encarnación Raymundo-Piñero, Juan I Paredes

$NbSe_2$ nanosheets/nanorolls obtained via fast and direct aqueous electrochemical exfoliation for high capacity lithium storage

Daniel F. Carrasco[a], Sergio García-Dalí[a,b], Silvia Villar-Rodil[a,*], José M. Munuera[a], Encarnación Raymundo-Piñero[b], Juan I. Paredes[a,*]

[a]*Instituto de Ciencia y Tecnología del Carbono, INCAR-CSIC, Francisco Pintado Fe 26, 33011 Oviedo, Spain*

[b] *CNRS, CEMHTI UPR3079, Univ. Orléans, 1D avenue de la Recherche Scientifique, 45071, Orléans, France*

* Corresponding author: silvia@incar.csic.es (S. Villar-Rodil),

* Corresponding author: paredes@incar.csic.es (J. I. Paredes)

Abstract

Layered transition metal dichalcogenides (LTMDs) in two-dimensional (2D) form are attractive for electrochemical energy storage, but research efforts in this realm have so far largely focused on the best-known members of such a family of materials, mainly MoS_2, $MoSe_2$ and WS_2. To exploit the potential of further, currently less studied 2D LTMDs, targeted methods for their production, preferably by cost-effective and sustainable means, as well as control over their nanomorphology, are highly desirable. Here, we report a quick and straightforward route for the preparation of 2D $NbSe_2$ and other metallic 2D LTMDs that relies on delaminating its bulk parent solid under aqueous cathodic conditions. Unlike typical electrochemical exfoliation methods for 2D materials, which generally require an additional processing step (e.g., sonication) to complete delamination, the present electrolytic strategy yielded directly exfoliated nano-objects, in a very short time (1-2 minutes) and with significant yields (~16 wt%). Moreover, the dominant morphology of the exfoliated 2D $NbSe_2$ products could be tuned between rolled-up nanosheets (nanorolls) and unfolded nanosheets, depending on the solvent where the nano-objects were dispersed (water or isopropanol). This rather unusual delamination behavior of $NbSe_2$ was explored and concluded to occur via a redox mechanism that involves some degree of hydrolytic oxidation of the material triggered by the cathodic treatment. The delamination strategy could be extended to other metallic LTMDs, such as NbS_2 and VSe_2. When tested toward electrochemical lithium storage, electrodes based on the exfoliated $NbSe_2$ products delivered very high capacity values, up to 750-800 mAh g^{-1} at 0.5 A g^{-1}, where the positive effect of the nanoroll morphology, associated to increased accessibility of the lithium storage sites, was made apparent. Overall, these results are expected to expand the availability of fit-

for-purpose 2D LTMDs by resorting to simple and expeditious production strategies of low environmental impact.

Keywords: Layered transition metal dichalcogenides (LTMDs); $NbSe_2$; VSe_2, electrochemical exfoliation; nanorolls; energy storage

1. Introduction

The emergence of graphene in 2004 signaled the beginning of the now vast field of two-dimensional (2D) materials, the breadth of which pertains to the large number of different known 2D systems, their possible combinations (2D heterostructures) and the exotic physical phenomena they can give rise to, as well as to the variety of technological domains where they can be potentially applied [1,2]. One such relevant domain is that of electrochemical energy storage (EES), where many 2D materials (typically, those having sufficient electrical conductivity) can be used as efficient electrodes for various types of supercapacitors [2] and batteries [3], including metal-ion, metal-sulfur and metal-air batteries. In addition to the distinct advantages that a given 2D system might exhibit on account of its particular chemical composition and structural configuration, 2D materials possess some overarching features that make them especially attractive for EES applications, most notably, high specific surface areas and extremely thin (usually <10 nm) sheet-like morphologies [3]. Such features are expected to be conducive to promoting charge storage by facilitating extensive interactions with, e.g., ions and redox-active species, as well as by expediting mass transport through the electrode, particularly when the thin sheets are of limited lateral dimensions (e.g., below a few micrometers).

Over the last decade, intensive research efforts have been made to unlock the full potential and advance the implementation prospects of 2D materials in EES devices [2–4]. However, these efforts have preferentially, although not exclusively, focused on a small subset of 2D materials, which mainly includes graphene and its derivatives [5], a few layered transition metal dichalcogenides (LTMDs), MXenes and Xenes (mostly MoS_2, $Ti_3C_2T_x$ and phosphorene, respectively) [6–8], as well as some 2D metal oxides and hydroxides [9]. Not surprisingly, many of them are readily accessible materials, with techniques for their production and processing in significant amounts being already relatively mature. Thus, to uncover the possibilities and exploit the promise of other, currently less explored 2D materials for EES, suitable targeted preparation methods should be developed in parallel [4]. Another relevant issue in the use of 2D materials as electrodes for EES concerns their actual nanomorphology and aggregation state in the electrode. 2D materials are often obtained in the form of stand-alone, largely unfolded nanosheets, e.g., in colloidal dispersion, but their processing into electrodes can easily lead to widespread nanosheet re-stacking and, consequently, to a dramatic decrease in the available surface area and to a deterioration of the ion diffusion kinetics [10]. This issue can be alleviated by, among other strategies, assembling the nanosheets into suitable nanomorphologies, such as loose aggregates (e.g., nanoflowers), hollow/porous structures (nanorolls, nanospheres, porous gels, etc), or highly crumpled films [11]. Therefore, straightforward approaches that allow access to these types of nanomorphologies with 2D materials are also highly desirable.

As a member of the 2D LTMD family, $NbSe_2$ nanosheets are a very attractive material for EES applications. Different to the case of the most commonly studied LTMDs, such as MoS_2, WS_2 and $MoSe_2$, which are electrically semiconducting compounds in their thermodynamically stable phase (2H phase), $NbSe_2$ exhibits a

metallic nature that should favor its use in such applications [12]. Indeed, although still rather limited in number, some reports have in recent years disclosed the potential of $NbSe_2$ nanosheets/nanostructures, either alone or in combination with other materials, as a suitable electrode for Li-ion [13–15], Na/K-ion [16–18] and multivalent-ion [13,19] storage in batteries, as well as for Li-S batteries [20] and supercapacitors [21,22]. However, also in contrast with the most widespread LTMDs, the pool of available methods for producing $NbSe_2$ nanosheets in significant amounts has so far remained quite small, which in turn has limited the range of practically available 2D $NbSe_2$ materials. For example, top-down methods essentially boil down to the well-known, generic exfoliation of the bulk material in proper organic solvents driven by ultrasound [23], and to electrochemical exfoliation with electrolytes based on lithium or alkylammonium salts, also in organic solvents [24–26]. Likewise, control over the nanomorphology of 2D $NbSe_2$ has been mainly restricted to nanoflower-like structures obtained by solvothermal synthesis [14]. Hence, strategies that allow access to $NbSe_2$ nanosheets as well as some control of their nanomorphology without resorting to the use of organic media (e.g., more sustainable, water-based strategies) would be an important asset to further the prospects of this material in EES and other applications.

Here, we report a straightforward approach for the production of $NbSe_2$ nanosheets via an electrochemical delamination route carried out in an aqueous electrolyte. We also show that, depending on the specific solvent where the exfoliated product is dispersed (water or isopropanol), the obtained nanosheets can be preferentially rolled-up into 1D nano-objects (nanorolls) or kept in an unfolded state. A mechanism based on redox processes is proposed to account for the somewhat unusual, smooth electrolytic delamination of the starting bulk $NbSe_2$ material. Such mechanism applies to other metallic LTMDs, allowing their straightforward delamination, as shown here for NbS_2

and VSe_2. Likewise, the 2D $NbSe_2$ nanorolls and unfolded nanosheets are both investigated as an electrode material for Li-ion storage, thus affording a direct comparison of the effect of nanomorphology on the EES performance. In particular, the nanorolls are seen to reach quite high Li-ion storage capacity values, making them a competitive anode material for Li-ion batteries. Thus, by introducing a simple, water-based method for producing 2D $NbSe_2$ with controlled nanomorphology, the present results should expand the scope of less studied LTMDs in EES and beyond.

2. Results and discussion

2.1. General aspects of the cathodic delamination of $NbSe_2$ in aqueous medium

An electrochemical delamination route was implemented for the preparation of $NbSe_2$ nanosheets from their corresponding bulk material in powder form [details of the procedure are given in the Experimental section (see Supporting Information)]. In an optimized procedure, a certain amount of commercial $NbSe_2$ powder (Fig. 1a), made up of micrometer- and submicrometer-sized particles [see field emission scanning electron microscopy (FE-SEM) image in Fig. 1b], was compacted onto a circular piece of graphite foil by means of a hydraulic press (Fig. 1c). The graphite foil served as an electrically conductive supporting substrate for the LTMD and acted as the cathode in an electrolytic set-up that made use of platinum foil as the anode. Both electrodes were immersed in an aqueous 0.3 M KNO_3 solution in a parallel configuration and kept at a distance of ~2 cm from each other (Fig. 1d). The side of the graphite foil coated with $NbSe_2$ was directly facing the platinum counter electrode. Upon application of a negative voltage (-10 V) to the $NbSe_2$-graphite foil electrode for a few minutes, lustrous gray particles were seen to detach from it and to quickly sediment at the bottom of the electrolytic cell. At the same time, a reddish-brown substance was also released from

the cathode surface, but this remained suspended in the electrolyte instead (Fig. 1e; see also Movie 1 in the Supporting Information). Such a substance, as well as the gray particles, necessarily originated from the $NbSe_2$ component of the cathode, because they were not observed when the naked graphite foil was negatively biased. The latter only underwent a slight swelling and released just a few black particles that floated atop the electrolytic solution (see Movie 2 in the Supporting Information). Indeed, aqueous cathodic delamination of graphite in significant extent is known to require treatments on the scale of hours, rather than minutes, and the use of more complex, specific electrolytes [27]. Moreover, both the reddish-brown substance and the gray particles were also generated when stand-alone, pressed $NbSe_2$ pellets were used as the cathode, i.e., in the absence of the graphite foil support (see Movie 3 in the Supporting Information). However, such stand-alone pellets were relatively brittle and thus more difficult to handle than their graphite foil-supported counterparts. After completion of the cathodic treatment in just a few minutes, the reddish-brown substance in the electrolyte was collected (the gray sediment discarded), washed with deionized water [three cycles of (i) sedimentation via centrifugation or overnight resting and (ii) re-suspension in water], dried under a vacuum at room temperature and then stored for further use. This product could be colloidally dispersed in isopropanol and water (Fig. 1f) with the aid of a vortex mixer or a brief (1 or 2 minutes) sonication step, although its stability was generally rather limited, with most of the material sedimenting in several hours. Nonetheless, the sediment could be easily re-suspended for an indefinite number of times, indicating that an irreversible agglomeration of the colloidally dispersed product was not taking place.

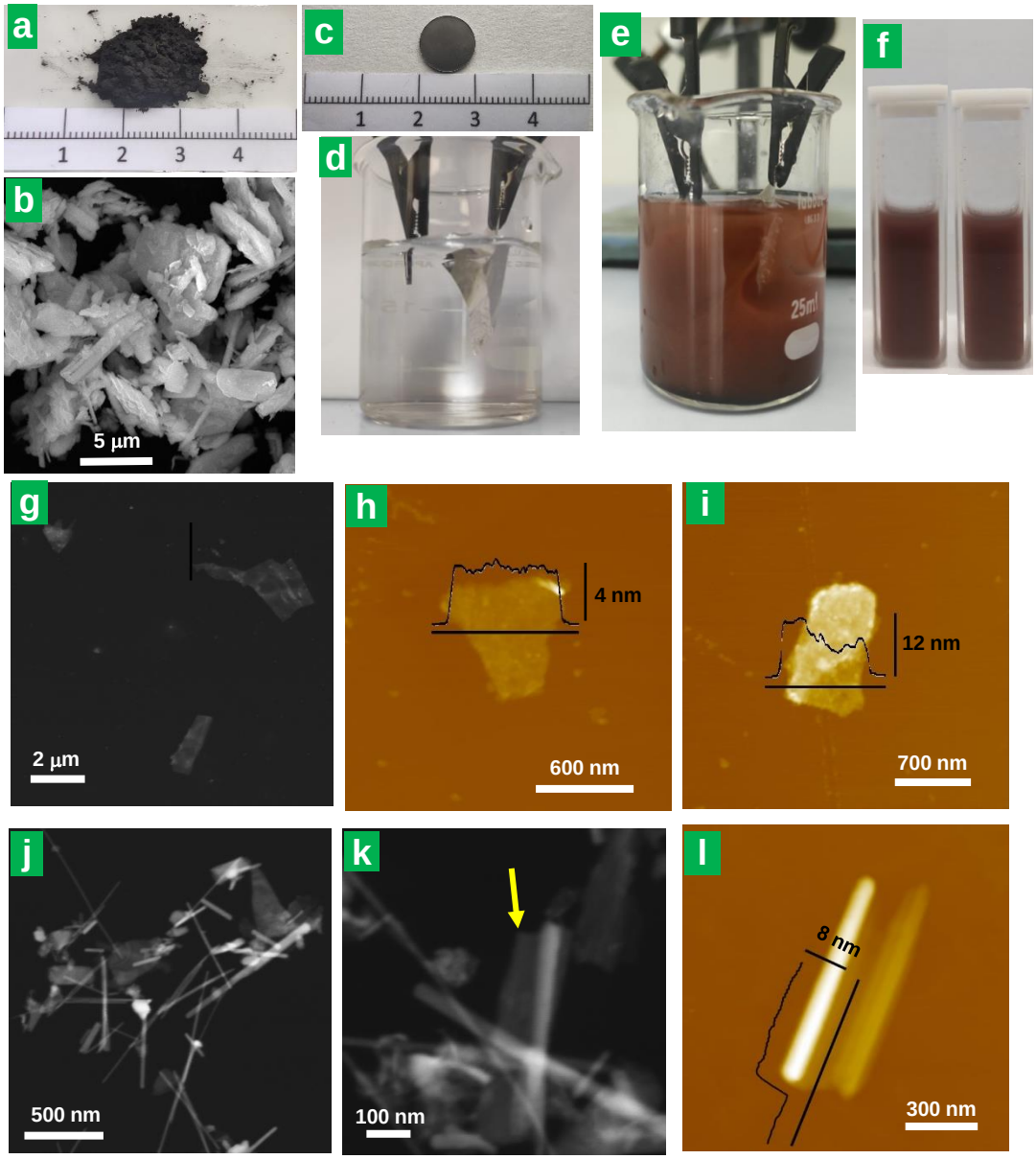

Figure 1. (a) Digital photograph and **(b)** FE-SEM micrograph of commercial $NbSe_2$ powder. Digital photographs of **(c)** the $NbSe_2$-graphite foil cathode and the experimental set-up for electrolytic exfoliation **(d)** before and **(e)** after application of a negative voltage (-10 V) to the $NbSe_2$-graphite foil cathode. **(f)** Digital photographs of the cathodic exfoliation product colloidally dispersed in isopropanol (left) and water (right). Typical STEM **(g)** and AFM images **(h,i)** and of the cathodically derived product deposited from its dispersion in isopropanol. **(j,k)** STEM images of the cathodic product

deposited from its dispersion in water. The arrow in k points to a site where the sheet is incompletely rolled-up**. (l)** AFM image of a partially unfolded nanoroll

Fig. 1g shows a typical scanning transmission electron microscopy (STEM) image of the cathodically derived product from its dispersion in isopropanol, where it can be noticed that the material was made up of submicrometer-sized nanosheets of irregular polygonal profile, showing lengths mostly in the ~300–600 nm range. As determined by atomic force microscopy (AFM; Figs. 1h and 1i), the nanosheets were typically between 4 and 12 nm in thickness. Based on the above observations, it is reasonable to conclude that these 2D objects were obtained from the delamination of bulk $NbSe_2$ during the cathodic treatment. If we assume 0.628 nm to be the thickness of a $NbSe_2$ monolayer [28], then the present nanosheets would be nominally several (~6–19) monolayers thick, according to the above AFM results (Figs. 1h and 1i). Nonetheless, this result will need to be refined in the light of further data, as discussed below. However, the actual morphology of the delaminated nano-objects could also be modulated by a proper selection of the dispersing solvent. Fig. 1j presents a STEM image of the cathodic product deposited from its dispersion in water, instead of isopropanol. In this case, while nanosheets were still spotted in significant numbers, the sample was largely dominated by 1D entities that were about 500–700 nm long and ~20 nm wide. Closer inspection of the 1D objects (Fig. 1k) revealed them to possess a tubular morphology and suggested that they were formed by the rolling-up of nanosheets to give nanorolls (note the incompletely rolled-up sheet at the site marked by an arrow in Fig. 1k). Further evidence of this point is given in the AFM image of Fig. 1l, where a partially unrolled nanoroll can be noticed. The two ends of the corresponding nanosheet appeared to be rolled up, with only its middle section unrolled. From the unrolled

section, the thickness of the nanosheet was estimated to be ~7–8 nm. It is worth noting that this nanosheet was initially fully rolled up (a single 1D object was seen during the first AFM scan, image not shown), but a partial unrolling apparently took place at some point of the measurement, likely as a result of perturbations induced by interaction with the AFM tip.

The transformation between unfolded nanosheet and nanoroll morphology of the present cathodically delaminated materials appeared to be reversible through solvent exchange. For example, the as-obtained, dried cathodic product first dispersed in isopropanol yielded unfolded nanosheets, but if isopropanol was exchanged by water (via several cycles of sedimentation by centrifugation and re-suspension in water), nanorolls became the dominant nanomorphology, and vice versa (see Fig. S1 in the Supporting Information). Not surprisingly, nanorolls were prevalent in the as-obtained, dried cathodic product that was not subsequently dispersed in any solvent (Fig. S2), given that this product was originally processed in water. It is also worth noting that such a solvent-driven control of the nanomorphology was not exclusive of the cathodically derived material. Indeed, direct sonication of bulk $NbSe_2$ powder in isopropanol and water also afforded suspensions made up of unfolded nanosheets and rolled-up nanotubes, respectively (Fig. S3). However, the cathodic delamination strategy turned out to be a much more efficient process than direct sonication. For instance, a delamination yield of ~16 wt% could be obtained with the cathodic process in just a few minutes (at the expense of just ~0.7 A h /g), whereas direct sonication only gave a yield of ~6 wt% after 6 hours. Generally speaking, it is not possible to establish a comparison in terms of delamination yield with previous examples of $NbSe_2$ electrochemical exfoliation in the literature, as this data is not usually reported [24,26].

In some instances, the efficiency of the exfoliation is discussed in terms of exfoliation degree, i. e., the percentage of monolayers obtained over the whole exfoliated material [26] but, of course, this does not allow to know which wt% of the starting material has been exfoliated. We note that the delamination yield of ~16 wt% found here could be further increased if, instead of discarding the gray sediment from the electrolytic exfoliation of $NbSe_2$ (which is none other but non-exfoliated $NbSe_2$), it was recovered and pressed again onto a graphite foil disc to be used again as anode in successive exfoliation cycles.

The effect of different electrolytic parameters on the amount of delaminated product was also investigated. Taking the 0.3 M KNO_3 electrolyte and bias voltage of -10 V as the benchmark treatment conditions, we observed that both lower (e.g., 0.1 M) and higher (e.g., 1 M) electrolyte concentrations clearly led to smaller amounts of delaminated products. In the former case, delamination was relatively slow and generated little reddish-brown substance in the aqueous solution. In the latter, a much more vigorous process was noticed, but this only resulted in a very quick detachment of gray particles that sedimented at the bottom of the solution, with no or very little reddish-brown substance being released. Under such conditions, the detaching particles probably loose their electrical contact to the cathode so quickly that there is virtually no time for them to delaminate to any significant extent. The magnitude of the bias voltage had a similar effect, so that both smaller (e.g., -5 V) and larger (e.g., -20 V) voltages gave rise to lower delamination efficiencies. The amount of delaminated product also decreased when changing the cation in the electrolyte from K^+ to Na^+ or Li^+, which was ascribed to the reduced ability of the latter ions in hydrated form to reach and intercalate the LTMD due to their lower ionic conductivity and larger size [27]. Changing the electrolyte anion to, e.g., Cl^- had no apparent effect on the delamination efficiency.

However, the use of anions that are highly oxidizing or can readily generate highly oxidizing species in the electrolyte should be avoided, as these could then attack the oxidation-prone $NbSe_2$ (see below). In this regard, the Cl^- anion can be expected to anodically oxidize during the electrolytic treatment, to give Cl_2 and then hypochlorous acid (HOCl) upon reaction with water, which is a rather oxidizing species. By contrast, the reduction potential of the NO_3^- anion is lower than that of HOCl (0.96 vs.1.48 V, relative to the standard hydrogen electrode) [29], making it a weaker oxidizing species and thus a better choice as the electrolyte anion for $NbSe_2$ exfoliation.

2.2. Physicochemical characterization of cathodically delaminated $NbSe_2$

The identity of the delaminated products was assessed by X-ray diffraction (XRD), Raman spectroscopy and X-ray photoelectron spectroscopy (XPS). Possessing different probing depths, each of these characterization techniques gathers partial information on the material, which must be combined to generate a global picture (see Fig. S4). The XRD pattern of the starting bulk $NbSe_2$ powder (Fig. 2a, black trace) exhibited an array of well-defined, sharp diffraction peaks that was consistent with the material being 2H-phase $NbSe_2$ (hexagonal crystal structure with space group $P6_3/mmc$) [30]. A couple of additional peaks, marked with an asterisk in the diffractogram, indicated the presence of elemental selenium of trigonal phase (t-Se) as an impurity in the material [31,32]. For $NbSe_2$, the strong (002) reflection located at ~14.10º (2θ) indicated the interlayer distance in the LTMD to be of 0.628 nm. Most, if not all, of the diffraction peaks characteristic of 2H-phase $NbSe_2$ were also present in the cathodically delaminated product, whether the latter was predominantly in the form of nanorolls (i.e., processed in water only; Fig. 2a, orange trace) or of unfolded nanosheets (upon processing in isopropanol; Fig. 2a, red trace). Some t-Se was also noticed in the XRD patterns of

some of the delaminated products. As will be explained below, although elemental Se is indeed present in the exfoliated products, it is not necessarily in crystalline t-Se form. It can be in amorphous, S_8 form, which is not detectable by XRD. Although the intensity of the (002) peak could be maybe expected to decrease relative to that of the other peaks upon exfoliation [30] (and finally disappear in the complete exfoliation, down to monolayer), the simultaneous decrease in the lateral size of the $NbSe_2$ entities will also diminish the intensity of the XRD peaks corresponding to other spatial directions, and thus the final effect in the relative intensities is not clear.

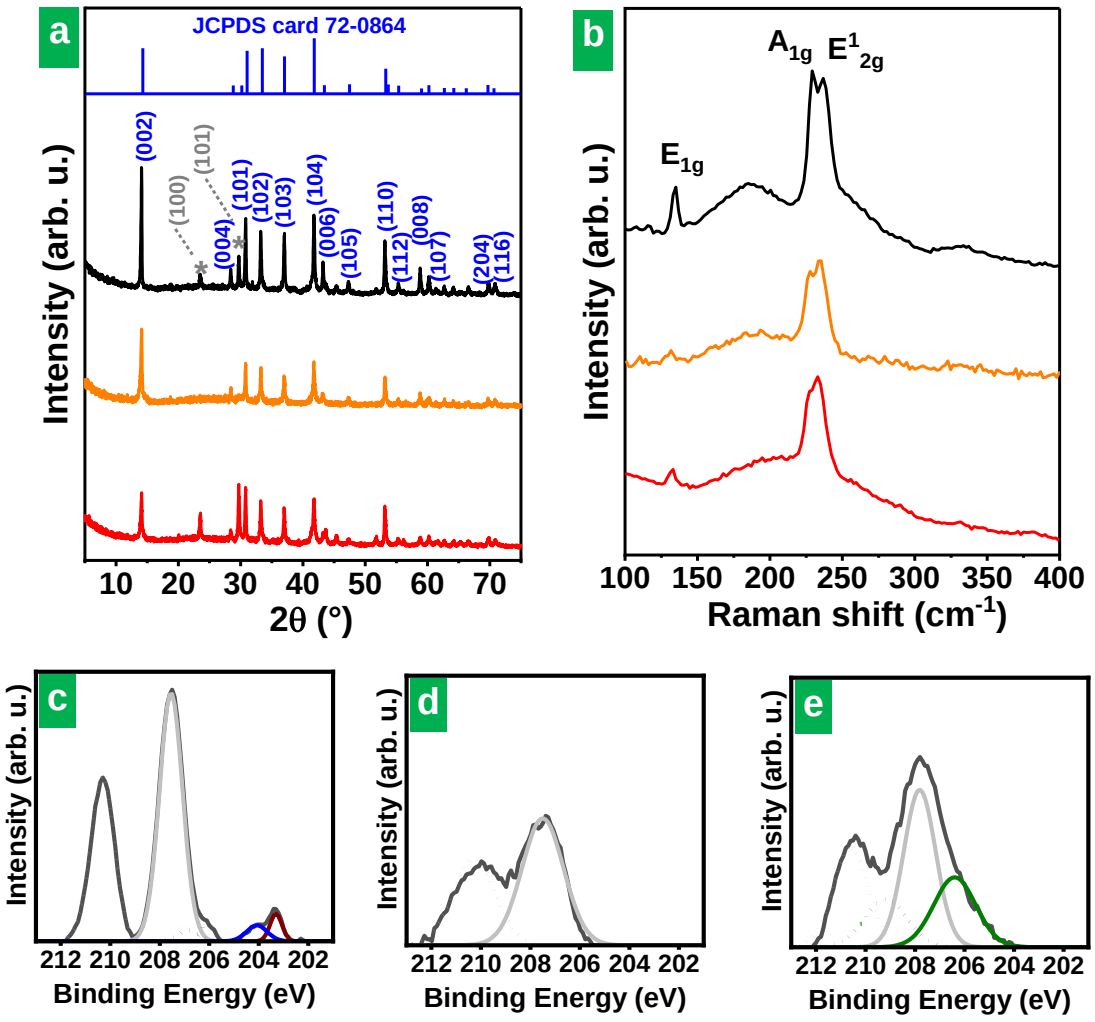

Figure 2. XRD pattern **(a)** and Raman spectrum **(b)** of the starting bulk $NbSe_2$ powder (black trace) and the cathodically delaminated product processed in water only (orange

trace) and in isopropanol (red trace). 2H-$NbSe_2$ XRD peaks have been labelled according to JCPDS card 72-0864 (blue trace and labels) while the peaks labeled in gray and marked with an asterisk correspond to crystalline selenium in trigonal phase, namely, to 2θ values of 23.5° and 29.7° corresponding to the crystal planes (100) and (101), respectively. Background-subtracted high-resolution Nb 3d XPS spectrum of **(c)** the starting bulk $NbSe_2$ powder and the cathodically delaminated product processed in **(d)** water only and **(e)** in isopropanol. Niobium appears in different oxidation states and/or chemical environments: Nb(V) from orthoniobates or polyoxoniobates (gray trace); Nb(IV) from $NbSe_2$ (wine trace) and in NbO_2 (green trace); Nb(II) in NbO (blue trace). The Nb $3d_{3/2}$ and Nb $3d_{5/2}$ components are graphed with solid and dotted lines, respectively.

Fig. 2b (black trace) shows a typical Raman spectrum of bulk $NbSe_2$ powder in the 100-400 cm^{-1} wavenumber range, where the characteristic bands (signature peaks) for the 2H phase of this LTMD are known to be located [33,34]. These include the intense and sharp A_{1g} (~230 cm^{-1}) and E^1_{2g} (~240 cm^{-1}) peaks, which correspond, respectively, to an out-of-plane vibrational mode of the chalcogen atoms and an in-plane vibrational mode of both the metal and chalcogen atoms. The weaker E_{1g} peak (~135 cm^{-1}) is an in-plane vibrational mode of the chalcogen atoms that is thought to be activated only at edge planes. In addition, a broad band that could be assigned to the so-called soft mode was noticed at about 180 cm^{-1}. The latter is a second-order feature involving two-phonon scattering processes and its relatively high intensity is connected to the fact that $NbSe_2$ exhibits charge density wave states at low temperatures [35,36]. These Raman bands have been shown to be also present, with very minor variations (e.g., a shift in peak positions of just a few cm^{-1}, if any), in atomically thin $NbSe_2$ [37,38]. In fact, such

bands were clearly noticed in the cathodically delaminated product obtained here, whether it was processed in water only or transferred to isopropanol (Fig. 2b, orange and red traces, respectively). Nonetheless, the Raman features of this product were largely but not totally coincident with those expected for (bulk or atomically thin) $NbSe_2$. Specifically, in the delaminated material, the peak at ~240 cm^{-1} (i.e., the E^1_{2g} band frequency of 2H-$NbSe_2$) was somewhat more intense than its 230 cm^{-1} counterpart (A_{1g} band frequency of 2H-$NbSe_2$), whereas this is not usually the case with the E^1_{2g} and A_{1g} bands for pure $NbSe_2$ (e.g., see the spectrum of bulk $NbSe_2$ in Fig. 2b) [33,35,37,38]. We interpret such distinct Raman feature of cathodically delaminated $NbSe_2$, relative to those expected for the pure LTMD, to arise from a partial oxidation of the obtained nanosheets/nanorolls. The surface of bulk $NbSe_2$ is known to slowly oxidize under ambient conditions, giving Nb(V) species, which are mainly thought to be amorphous Nb_2O_5, and elemental Se [3940]. This reaction can be accelerated with external stimuli, such as heat or light [41,42]. Surface oxidation readily develops on 2D $NbSe_2$ nanosheets as well [43,44]. Moreover, as will be shown below, the present cathodic treatment of $NbSe_2$ leads to the surface oxidation of the delaminated objects. However, the unusual Raman features of the delaminated products cannot be ascribed to the presence of Nb_2O_5, either in crystalline or in amorphous form (see Fig. S5). In fact, Nb_2O_5 exhibits other intense features outside the 100-400 cm^{-1} range, particularly strong bands at around 600–700 cm^{-1} [45], which we detected in commercial samples of both crystalline and amorphous Nb_2O_5, but not at all in the cathodically delaminated $NbSe_2$ material (see Fig. S5). Instead, the unusual Raman features of the delaminated products most likely arise from elemental Se species as the other product of $NbSe_2$ oxidation. In fact, the Raman spectrum of t-Se, which was detected here by XRD (Fig. 2a), is known to be dominated by a band at 235-240 cm^{-1} (A_1 vibrational mode), whereas Se_8 rings in

amorphous Se (a-Se) give rise to a peak at around 260 cm^{-1} (intra-ring stretching vibrations) [46,47]. Elemental Se, both in crystalline and amorphous form, was therefore very likely responsible for the slightly altered Raman features of cathodically delaminated $NbSe_2$ (a Raman spectrum of elemental selenium will be shown below regarding the discussion of the exfoliation mechanism).

Some (native) surface oxidation was also expected on the starting bulk $NbSe_2$ particles, but the thickness of the corresponding layer of oxidation products was probably small compared to the probing depth of the Raman technique (a few tens of nanometers for $NbSe_2$ [33]). For this reason, the intensity of the Raman features resulting from such products (i.e., those of elemental Se) in bulk $NbSe_2$ was negligible relative to those coming from the LTMD proper (Fig. 2b, black trace). In the delaminated materials, the amount of surface oxidation products probed relative to that of (non-oxidized) $NbSe_2$ should be considerably larger due to the nanometric thickness of the nanosheets/nanorolls. Hence, their Raman bands should be easier to detect (Fig. 2b, orange and red plots). In agreement with previous work [48], further oxidation of the delaminated nanosheets/nanorolls could be triggered by repeatedly measuring a given area with the Raman laser beam. This effect was clearly noticed from the progressive rise of the 240 and 260 cm^{-1} peaks when spectra were consecutively recorded on the same spot (not shown). In consequence, to avoid altering the exfoliated samples throughout the measurements, the spectra were obtained with low laser powers (below 0.5 mW) and short measurement times (a few tens of seconds).

The presence of a surface layer of oxidation products both on the starting bulk $NbSe_2$ powder and on its cathodically delaminated counterpart was disclosed by a much more surface-sensitive technique (smaller probing depth), namely, X-ray photoelectron spectroscopy (XPS). The high-resolution core-level Nb 3d spectra of the bulk powder as

well as of the exfoliated nanorolls and nanosheets are presented in Fig. 2c, d and e, respectively. In all cases, the spectral envelopes were dominated by components located at ~207.5 and ~210.2 eV (gray traces in Figs. 2c–e), which can be assigned to the $3d_{5/2}$ and $3d_{3/2}$ levels of Nb(V), respectively, and were thus indicative of Nb oxide species on the surface of the samples [19]. Much weaker features consistent with 2H-phase $NbSe_2$, i.e., the components located at about 203.2 [Nb(IV) $3d_{5/2}$] and 206.0 [Nb(IV) $3d_{3/2}$] eV [19], were observed in the spectrum of the bulk powder (wine traces in Fig. 2c). Niobium oxides with oxidation states lower than V were also detected (blue and green traces in Fig. 2c and e, respectively). This result agrees with previous reports in the literature on XPS characterization of $NbSe_2$ nanosheets where Nb(V) is either the only [14] or the majoritarian component detected [24] in the Nb 3d spectrum. The core-level O 1s spectra of these materials was consistent with most of the surface Nb being in the form of oxide, e.g., orthoniobates, polyoxoniobates or Nb_2O_5 (Fig. S6). In agreement with the detection of elemental Se by XRD and Raman spectroscopy (Fig. 2a and b), XPS also revealed the presence of this species in the bulk and delaminated materials (see Se 2p core-level spectra in Fig. S7).

In the case of the delaminated nanosheets/nanorolls, we assume that the surface layer of oxidation products mostly formed during their preparation by the cathodic treatment (see below). Moreover, it can be inferred that just one or two of the outermost monolayers in the $NbSe_2$ nanosheets (as well as their rolled-up counterparts) eventually got oxidized to give Nb oxide and elemental Se species on the surface. These oxidized layers would sandwich an inner section containing a few or several non-oxidized $NbSe_2$ monolayers. Such a conclusion was mainly supported by two facts. First, the thickness of the delaminated nanosheets was in the 4–12 nm range. Second, upon oxidation, the thickness of $NbSe_2$ slabs/nanosheets has been shown to increase substantially, up to a

factor of ~3 [41,48]. Hence, considering that a pristine $NbSe_2$ monolayer is ~0.6 nm thick [28], the layer of oxidation products in the delaminated nanosheets should not have originated from, e.g., the three outermost $NbSe_2$ monolayers, as these would have led to nanosheets considerably thicker than those actually measured here. Rather, the nanosheet thickness would be consistent with such an oxidation layer coming from one or two $NbSe_2$ monolayers. Moreover, the thickness of this oxidation layer (i.e., a few nanometers) would be similar to values given in the literature for the native oxide in 2D $NbSe_2$ and NbS_2 nanostructures [49,50], as well as to the typical probing depth of the XPS technique [51], implying that most, if not all, of the XPS signal should originate from the oxidation layer (see Fig. S4), as demonstrated in Figs. 2c–e and reported in previous works on $NbSe_2$ nanosheets [14,24]. However, as explained above, the deeper probe depth of a few tens of nanometers of Raman spectroscopy will allow detecting both the oxide layer and the 2H-$NbSe_2$ core of a number of thin nanosheets (4-12 nm thick, see Fig. 1h and 1i) constituting the probed films (see Fig. S4), while less proportion of oxide layer (presumably only one oxidized surface) will contribute to the Raman signal for thicker, unexfoliated starting $NbSe_2$ powder (Fig. 2b). The larger probe depth of XRD will allow detecting the surface oxide layer and the unmodified 2H-$NbSe_2$ core for both the exfoliated objects and the starting powders (Fig. 2a and S4). We note that the presence of an oxidation layer is not avoided by using lower voltages for the electrochemical delamination, as the layer is present even in the case of the starting, non-electrochemically treated material. In fact, in previous reports in the literature for the case of electrochemical exfoliation of $NbSe_2$ in organic media, even when the electrochemical parameters were adjusted to minimize structure degradation, the main Nb species detected by XPS was still Nb(V) [24].

2.3. Rationalizing the aqueous cathodic delamination of $NbSe_2$ and the morphology of the delaminated products

The above results demonstrate that bulk $NbSe_2$ can be readily exfoliated by electrochemical means based on a simple and expeditious aqueous process, to give nanometer-thick nanosheets that can be switched between unfolded and rolled-up morphologies. We note that, while the protocols reported in the literature for the preparation of nanostructured $NbSe_2$ take hours [13,14,16–19] or even days [15], the duration of the present methodology is in the order of minutes. Indeed, after just two minutes of cathodic treatment, bulk $NbSe_2$ is transformed into well-exfoliated 2D $NbSe_2$ nano-objects (Fig. 1) with high structural quality (Fig. 2). Furthermore, unlike other methodologies, the present protocol is performed at room temperature and ambient conditions, not involving high temperatures [14,16–19], inert atmosphere [14,16,17,19] or complex or scarce reagents or solvents [18]. Significantly, the final individual exfoliated nano-objects could be directly obtained from the electrochemical treatment without the need of any further substantial energy input (e.g., sonication). Such an outcome was quite different to that found for typical electrochemical exfoliation methods of most layered materials, such as graphite, black phosphorus and LTMDs, including $NbSe_2$ itself. In those cases, the electrolytic treatment usually affords just a bulk expanded material (e.g., worm-like expanded particles or accordion-like expanded crystals), from which individual nanosheets need to be subsequently extracted in the liquid phase via, e.g., sonication or shear forces [52,53]. In contrast, no expanded particles were generated by the present electrochemical treatment of the bulk $NbSe_2$ powder. Indeed, FE-SEM imaging of the gray particles that sedimented at the bottom of the electrolytic cell during the treatment (not shown) showed them to be as compact as those of the starting material (Fig. 1b). This suggested that delamination in the present

case did not proceed through simultaneous intercalation/expansion of many interlayer galleries in the $NbSe_2$ particles, which is the expected exfoliation pattern for common electrochemical methods, but rather via a sequential, layer-by-layer peeling process. The latter would be more similar, although probably not identical, to the exfoliation behavior brought about by direct sonication of the bulk material. However, as noted above, the electrolytic exfoliation rate of $NbSe_2$ was much faster than that afforded by direct sonication. These observations pointed to an unusual exfoliation mechanism taking place here, which was thus worth examining.

We hypothesize that the present electrolytic exfoliation of $NbSe_2$ proceeded via a singular path akin to the redox mechanism of LTMD exfoliation proposed in recent years [54,55]. Such a redox exfoliation has been shown to rely on the generation of soluble molecular metal oxide precursors (e.g., orthometalates) on the surface of the LTMD particles, including $NbSe_2$, either via naturally occurring oxidation processes under ambient air or by purposeful oxidation with a chemical oxidant. Subsequent reduction of these soluble orthometalates yields the corresponding polyoxometalates. The latter are highly charged polyatomic anions that adsorb on the surface and at the interlayer gaps of the LTMD, triggering its sequential delamination through Coulombic repulsions with just a very small energy input (e.g., stirring) being required. This mechanism provides a priori a consistent conceptual framework to understand the aqueous electrolytic exfoliation of $NbSe_2$. Specifically, oxidation-prone $NbSe_2$ could certainly provide an abundant source of naturally occurring orthoniobate anions when the starting bulk material has been stored in the ambient air, as it was the case here. Indeed, the XPS results shown in Fig. 2c provided evidence of the presence of oxidized Nb species in the starting $NbSe_2$ powder. It could be argued that, under the intrinsically reductive conditions of the present cathodic treatment, the orthoniobate anions would

assemble into polyoxoniobates, and then the latter would drive the sequential exfoliation of the $NbSe_2$ particles as discussed above. This delamination process would be assisted by the intercalation of K^+ ions at $NbSe_2$ edges [27], affording a wedge effect that would facilitate the adsorption of orthoniobates and polyoxoniobates at interlayer gaps.

It should be noted, however, that the redox mechanism of LTMD exfoliation was not originally proposed in the context of either electrolytic or aqueous systems [54,55]. Consequently, different aqueous electrochemical processes that were previously not contemplated may have contributed to the currently observed outcome. In fact, we believe that during the aqueous cathodic treatment of $NbSe_2$, new oxidized Nb species are continuously generated in situ, facilitating the sequential delamination of the material. In such a scenario, the native Nb oxides already present in the starting bulk powder would not be strictly necessary to make exfoliation possible. To show evidence of this point, the starting $NbSe_2$ powder was subjected to reflux in acetonitrile with the aim of removing its native molecular Nb oxide species (this solvent is known to solubilize molecular metal oxide precursors present in LTMDs, including $NbSe_2$ [54,55]). Then, the refluxed $NbSe_2$ material was tested in an aqueous cathodic delamination experiment. If the native molecular Nb oxide species were strictly required for delamination to occur, the yield of exfoliated products obtained with the acetonitrile-treated $NbSe_2$ powder should be substantially lower, if not negligible, relative to that attained with its non-treated counterpart. Nonetheless, essentially the same yield was obtained in both cases (i.e., ~16 wt%), suggesting that in situ generated Nb oxide species are indeed central to the exfoliation process.

The generation of Nb oxide species during cathodic delamination most likely resulted from the pH-dependent hydrolytic oxidation of $NbSe_2$, and more specifically

hydrolysis under basic conditions. We note that due to the high bias voltage applied to the electrolytic cell, water molecules are expected to be reduced at the cathode side, yielding hydrogen molecules and hydroxide anions that raise the local pH of the aqueous electrolyte around the cathode. To demonstrate that a basic medium triggers the hydrolytic oxidation of $NbSe_2$, a control experiment was carried out whereby bulk $NbSe_2$ powder was stirred in a 3 M KOH solution (pH ~14) at 90 ºC for 30 min. Upon completion of the treatment, a very small amount of gray particles were seen to sediment at the bottom of the beaker and the supernatant solution developed a transparent dark red tone. The material in the supernatant was recovered by flocculation induced by the addition of HCl, washed through several cycles of centrifugation and re-suspension in water, and finally dried under vacuum. The resulting material was a dark red powder with a small amount of brilliant gray particles (see digital photograph in the inset to Fig. 3a and FE-SEM image in the same figure) with a weight that amounted to ~92-94 % of that of the starting bulk $NbSe_2$ powder. The gray particles that made up the sediment were also collected and washed, but their weight was just a few percent of the initial mass of $NbSe_2$ used for the treatment with alkali. XRD confirmed the presence of $NbSe_2$ in the gray particles (pattern not shown). In contrast, no sign of the LTMD was noticed in the XRD pattern of the powder coming from the supernatant, where just elemental Se could be detected (Fig. 3b). We note that the XRD pattern should come from the gray, crystalline Se allotrope, as the red allotrope is amorphous and is thus not detected by XRD. The latter result was supported by Raman spectroscopy (Fig. 3c), as only the characteristic peaks of (crystalline gray and amorphous red) elemental Se were seen in this material, but not those typical of $NbSe_2$. Still, Se was not the sole element present in the dark red powder: energy-dispersive X-ray (EDX) spectroscopy (Fig. 3d) revealed that it also contained substantial amounts of Nb (9–24 at%) and O (19–40

at%), together with some residual K and Cl (~1–2 at%) from the KOH and HCl solutions. Because Se was only found in its elemental form, we infer that O must be combined with Nb, thus forming Nb oxide species.

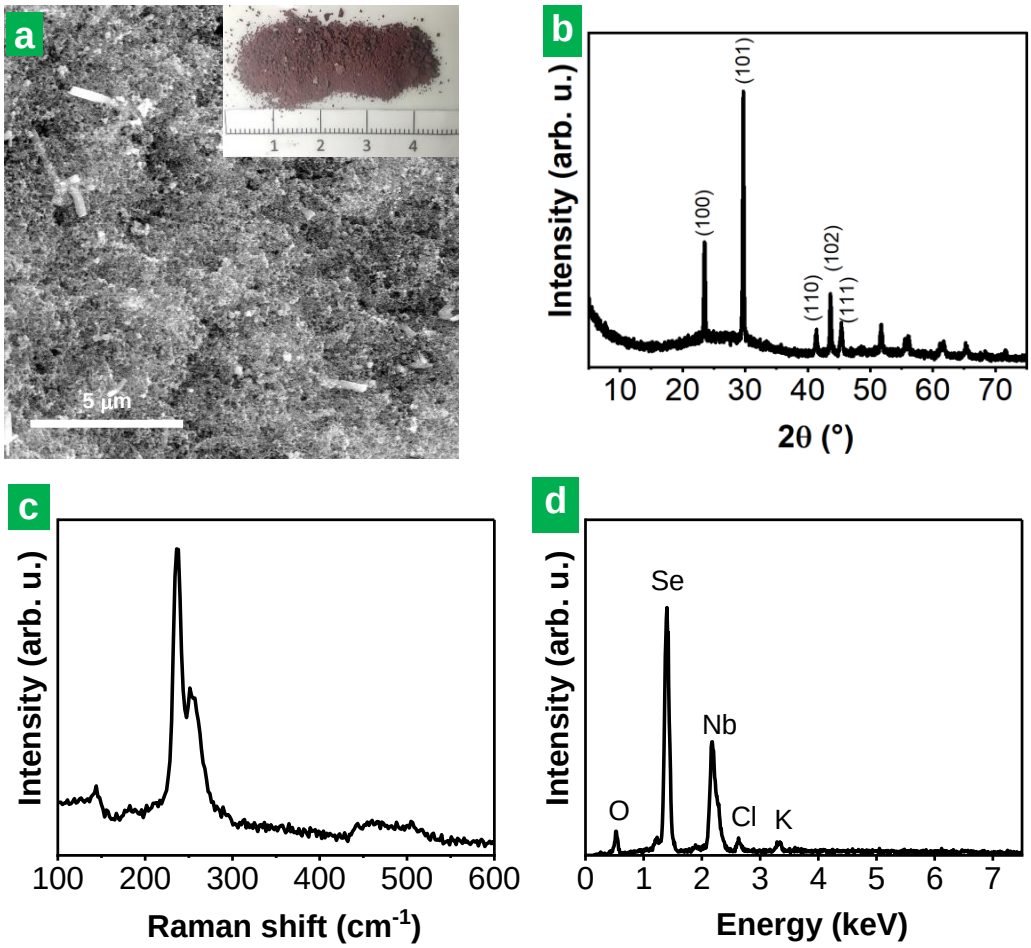

Figure 3. Characterization of the product of the treatment of bulk $NbSe_2$ powder with 3 M KOH solution (pH ~14) at 90 ºC for 30 min: **(a)** FE-SEM image with digital photograph in the inset, **(b)** XRD, **(c)** Raman, and **(d)** EDX. The XRD patterns obtained show the main peaks characteristic of crystalline t-Se at 2θ values of 23.5°, 29.7°, 41.4°, 43.7° and 45.4° corresponding to the crystal planes (100), (101), (110), (102) and (111), respectively, which have been labelled for clarity.

The above results demonstrate that, under basic conditions, $NbSe_2$ undergoes hydrolytic oxidation to give elemental Se and Nb oxide species. Moreover, the alkaline treatment can be made harsh enough to induce an almost complete decomposition of the material. Further hydrolysis experiments carried out at lower KOH concentrations indicated that substantial decomposition of $NbSe_2$ only occurred above a threshold pH value of about 10.5. Based on this new understanding and the general mechanism of redox exfoliation of LTMDs, the following course of events can be proposed for the aqueous cathodic delamination of $NbSe_2$: (1) Under the applied cathodic potential (-10 V), water molecules are reduced at the $NbSe_2$ electrode, thus raising the local pH of the electrolyte in a region close to the electrode surface, from an initial value of ~6 (pH of 0.3 M KNO_3 solution). (2) The local basic medium induces some degree of hydrolytic oxidation of the $NbSe_2$ surfaces that are in contact with the electrolyte, if they were not previously oxidized. Such an oxidation generates molecular Nb oxide species, most likely in the form of polyoxoniobates [e.g., the hexaniobate anion $(Nb_6O_{19})^{8-}$ referred to as the Lindqvist ion], rather than the monomeric orthoniobate anion, NbO_4^{3-}. This is because the latter is not stable in aqueous medium, whereas polyoxoniobates like the Lindqvist ion are known to readily form under alkaline conditions (pH >10.5) [56]. (3) An initial cathodic intercalation of K^+ ions, probably as hydrated entities ($[K(H_2O)_n]^+$ [27]), takes place at layer edges of the $NbSe_2$ particles, making the interlayer space at such edges to become exposed to the aqueous electrolyte, which triggers its oxidation. The resulting highly charged polyoxoniobates adsorb on the two opposite surfaces of the interlayer space, generating a strong electrostatic repulsion between them that causes their separation [54,55]. This event initiates delamination proper of a sheet at its edges. The assisting role of K^+ ions in the process explains the previously reported influence of KNO_3 concentration in the delamination yield (section 2.1). (4) The incipient

delamination of the sheet favors the ensuing intercalation of K^+ ions and the oxidation of the interlayer space at locations increasingly farther away from the edges. As a result, the sheet is progressively delaminated. (5) When delamination is completed, the sheet is released into the aqueous medium and a freshly exposed surface is ready for new exfoliation events. The very nature of the process entails the oxidation of both surfaces of the exfoliated sheets.

The delamination mechanism proposed here implies that the yield of exfoliation should be dependent, in a non-monotonous way, on the local pH of the electrolyte in the region close to the $NbSe_2$ cathode. Although this local pH could not be measured, its actual value during the cathodic treatment was probably not very far from the threshold of 10.5 that was shown above to trigger the hydrolytic oxidation of $NbSe_2$ and is also known to allow the solubilization of polyoxoniobates [56]. If it had been much lower than 10.5, no or little hydrolytic oxidation of $NbSe_2$ would have occurred, and so not many polyoxoniobates would have formed to support sheet delamination. As a result, a low exfoliation yield would have been expected. On the other hand, an exceedingly basic local pH would have likely driven a much too aggressive oxidation of the exposed $NbSe_2$ sheets, which would have extensively decomposed into elemental Se and Nb oxide species. Consequently, smaller amounts of $NbSe_2$ would have been available for delamination, thus leading to lower exfoliation yields. To test this prediction, the local pH around the $NbSe_2$ cathode should be controlled. While this is not possible by direct means, some indirect control should be feasible by tuning the pH of the starting electrolyte. To that effect, we conducted additional cathodic delamination experiments using purposefully acidified and basified electrolytes. More specifically, we prepared an acidic (pH ~1) and a basic (pH ~11) electrolyte by adding a proper amount of HNO_3 and KOH, respectively, to the standard 0.3 M KNO_3 neutral electrolyte, which gave

exfoliation yields of ~6 wt% (acidic) and ~11 wt% (basic). This result is to be compared with the yield of ~16 wt% obtained with the standard KNO_3 electrolyte (pH ~6) and is therefore consistent with the predictions derived from the proposed delamination mechanism.

The second relevant feature of the exfoliated $NbSe_2$ material was the fact that it could be obtained in the form of rolled-up nanosheets (nanorolls). This feature was not exclusive of the present electrolytic delamination process: as noted above, nanorolls could be generated as well just by sonicating the starting $NbSe_2$ powder in water, albeit at much lower yields. Moreover, different 1D $NbSe_2$ nanostructures, such as nanorods and nanowhiskers, have been previously generated by the processing of bulk $NbSe_2$ via, e.g., sonication or ball milling [57,58]. However, the origin of such a behavior is not clear. Nanoscrolls of several other LTMDs (MoS_2, $MoSe_2$, WS_2, etc) have been reported in recent years [59–62], but their preparation typically relies on the post-processing of the LTMD already in 2D form, not in bulk form. Indeed, the attainment of 1D nano-objects directly from the exfoliation of the bulk material has been rarely documented for LTMDs other than $NbSe_2$ [63,64]. It is thus reasonable to conclude that the ability of bulk $NbSe_2$ to yield 1D nano-objects directly upon exfoliation should be connected to some particular traits of this LTMD. We believe that the relatively strong tendency of $NbSe_2$ to oxidize (stronger than that of many other LTMDs) plays a central role. Specifically, the surface oxidation of the exfoliated $NbSe_2$ nanosheets is thought to generate stress in their structure in a way similar to the surface stress brought about by the adsorption of organic molecules (ligands) onto colloidal nanoplatelets, including LTMD nanosheets, which drives their folding into curved morphologies [62,65]. In this scenario, it is reasonable to assume that such a surface stress may be affected by the interaction of the oxide layer with its surrounding medium, and so that the induction of

curvature in the nanosheets depends on the solvent where they are dispersed. For the cathodically delaminated material, the required surface oxide species would be generated in situ, as discussed above. On the other hand, for the material obtained by direct sonication only the native surface oxides would be in principle available to support exfoliation and folding into 1D nanorolls, which would explain its lower yield. However, it should be possible to increase the exfoliation yield by generating oxide species in situ in this case as well, provided that the sonication treatment is carried out under proper alkaline conditions. To this end, we sonicated bulk $NbSe_2$ powder at different basic pH values, controlled by the addition of KOH. As could be anticipated, the exfoliation yield increased substantially when working at pH values of ~10–11, once again confirming the key part played by hydrolytic oxidation in the delamination behavior of this LTMD.

Finally, we demonstrated that the cathodic exfoliation route developed here for $NbSe_2$ could be extended to other LTMDs. To this end, metallic LTMDs such as NbS_2 or VSe_2 seemed to be better candidates than their semiconducting counterparts (MoS_2, WS_2, $MoSe_2$, etc) for two reasons. First, for the present exfoliation strategy to succeed, the LTMD should be highly reactive towards oxidation, particularly alkaline hydrolytic oxidation. By their own nature, metallic LTMDs are generally expected to be more prone to oxidation than semiconducting ones [66]. Second, the higher electrical conductivity of metallic LTMDs should favor the occurrence of the processes that lead to their exfoliation under electrolytic conditions. Such processes should be much more limited for semiconducting LTMDs as a result of their lower conductivity. Indeed, upon application of a negative voltage (-10 V), bulk NbS_2 and VSe_2 resulted in, respectively, gray and brownish-red colloidal dispersions (see Movie 4 and Fig. S8a for NbS_2, and Movie 5 and Fig. S8b for VSe_2 in the Supporting Information) of micrometer- and

submicrometer-sized 2D NbS_2 and VSe_2 nanosheets (see Fig. S8c and S8d in the Supporting Information, respectively). Thus, we have shown that the present simple and fast exfoliation strategy of low environmental impact is applicable to metallic LTMDs, making metallic 2D LTMDs available for, e. g., electrochemical energy storage.

2.4. Lithium storage performance of the cathodically delaminated $NbSe_2$ materials

The Li storage performance of the two cathodically delaminated $NbSe_2$ products, i.e., nanorolls and unfolded nanosheets, was evaluated in a half-cell configuration, with the $NbSe_2$ material combined with a conductive additive (a mixture of carbon black and carbon nanotubes) and a binder as the working electrode, Li metal foil as the counter and reference electrode, and 1 M $LiPF_6$ solution in an ethylene carbonate/diethylene carbonate solvent mixture (1/1 weight ratio) as the electrolyte (see Experimental section in the Supporting Information for details). We note that the two cathodically delaminated $NbSe_2$ products were not dispersed as individual objects in any solvent after their preparation and were thus expected to retain their different morphology though their testing as electrodes. Indeed, as will be seen below, their dissimilar electrochemical performance gave experimental indication of the persistence of such morphological difference. Fig. 4a and b shows the first four cyclic voltammograms (CVs) recorded for the rolled-up nanotubes and unfolded nanosheets, respectively, at a scan rate of 0.1 mV s^{-1} in the potential range 0.01–3.00 V vs. Li/Li^+. The CVs of both samples were qualitatively identical and, in agreement with previous reports, they were dominated by a number of redox features characteristic of $NbSe_2$ materials, where Li storage is thought to arise from a combination of intercalation and conversion processes [13–15]. Specifically, in the first cathodic scan (red trace, negative current range), the peaks located at ~1.64–1.67 and 1.47 V vs. Li/Li^+ have been ascribed to a transition of

the $NbSe_2$ lattice from the starting H phase to the H´ phase upon Li intercalation (i.e., xLi + H-$NbSe_2$ → Li_xH´-$NbSe_2$), as well as to the conversion of $NbSe_2$ into Li_2Se and metallic Nb (4Li + H-$NbSe_2$ → 2Li_2Se + Nb). Further, the relatively broad cathodic peak at 0.63 V vs. Li/Li^+ is thought to result from the conversion reaction of H´-phase $NbSe_2$ [Li_xH´-$NbSe_2$ + (4-x)Li → 2Li_2Se + Nb], whereas the sharp, intense peak at ~0.15 V vs. Li/Li^+ can be traced to the irreversible formation of a solid-electrolyte interphase (SEI) at the $NbSe_2$ electrode. In the ensuing anodic scan (red trace, positive current range), the relatively featureless, low-current ~0.05–1.50 V vs. Li/Li^+ region can be attributed to the conversion of Li_2Se and Nb back to Li-intercalated $NbSe_2$ [2Li_2Se + Nb → Li_xH´-$NbSe_2$ + (4-x)Li], while the sharp peaks at 1.86–1.88 and 2.23–2.25 V vs. Li/Li^+ have been attributed, respectively, to delithiation of $NbSe_2$ [Li_xH´-$NbSe_2$ → H´-$NbSe_2$ + xLi] and to oxidation of Li_2Se to give lithium polyselenides and/or elemental Se [e.g., $n$$Li_2Se$ → Li_2Se_n + 2(n-1)Li, with $4 \leq n \leq 8$]. The latter chemical species are then expected to reduce back to Li_2Se during the following cathodic scan (orange trace), which was indeed reflected in the peak appearing at 2.00–2.02 V vs. Li/Li^+. Significantly, this peak was already noticed in the first cathodic run of both samples, thus supporting the above conclusion that some elemental Se was present in the as-prepared delaminated $NbSe_2$ materials. The intensity of the peaks associated to intercalation/conversion processes in $NbSe_2$ decreased after the first CV, which suggested that such processes were not totally reversible.

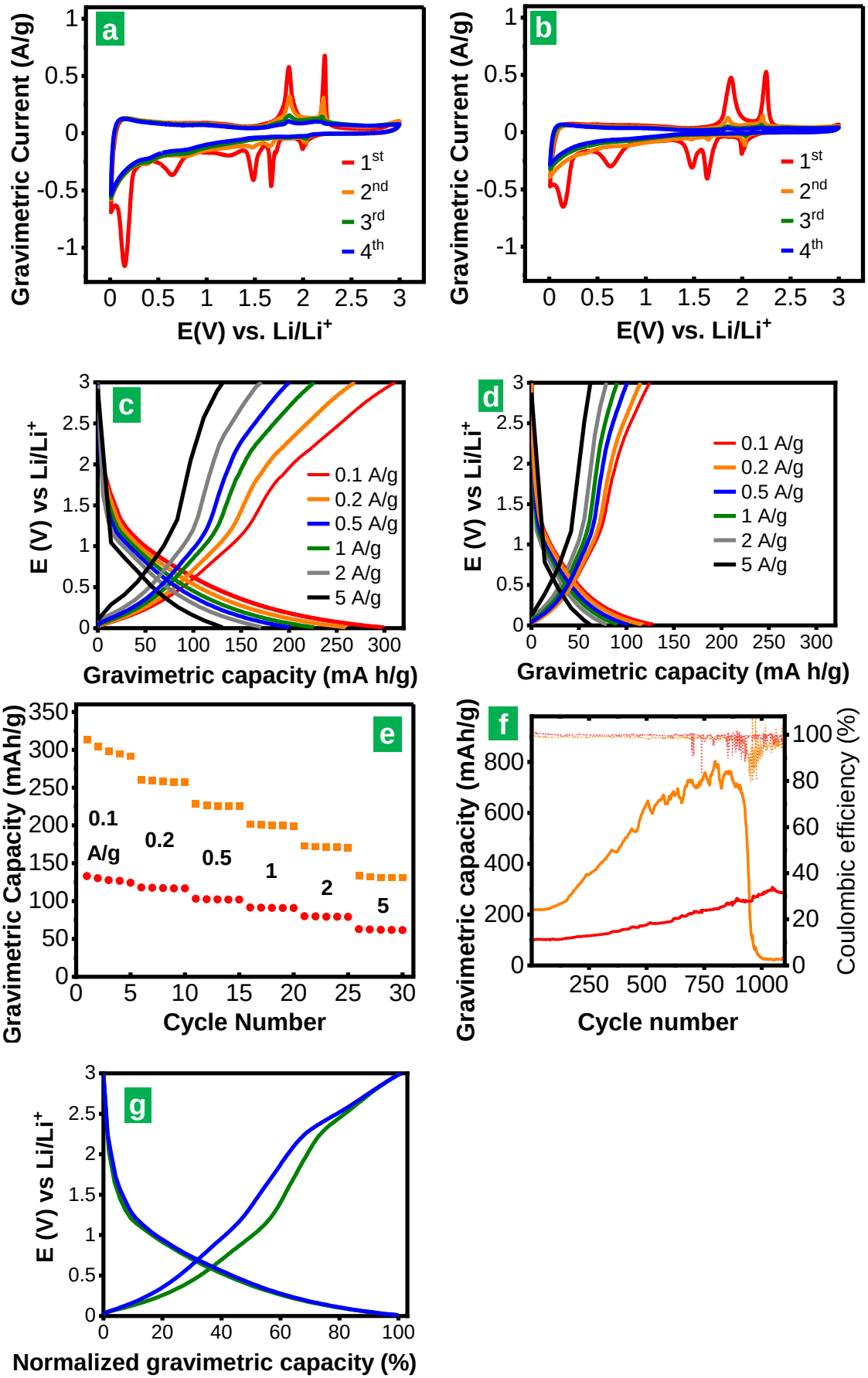
a
Gravimetric Current (A/g)
E(V) vs. Li/Li+
1st
2nd
3rd
4th
b
Gravimetric Current (A/g)
E(V) vs. Li/Li+
1st
2nd
3rd
4th
c
E (V) vs Li/Li+
Gravimetric capacity (mA h/g)
0.1 A/g
0.2 A/g
0.5 A/g
1 A/g
2 A/g
5 A/g
d
E (V) vs Li/Li+
Gravimetric capacity (mA h/g)
0.1 A/g
0.2 A/g
0.5 A/g
1 A/g
2 A/g
5 A/g
e
Gravimetric Capacity (mAh/g)
Cycle Number
0.1
A/g
0.2
0.5
1
2
5
f
Gravimetric capacity (mAh/g)
Coulombic efficiency (%)
Cycle number
g
E (V) vs Li/Li+
Normalized gravimetric capacity (%)

Figure 4. First four CVs for $NbSe_2$ nanorolls **(a)** and unfolded nanosheets **(b)** at a scan rate of 0.1 mV s^{-1}: 1st (red trace), 2nd (orange), 3rd (green), and 4th (blue). Typical GCD profiles for $NbSe_2$ nanorolls **(c)** and nanosheets **(d)** at current densities between 0.1 and 5 A g^{-1}. **(e)** Gravimetric capacity values for $NbSe_2$ nanorolls (orange squares) and nanosheets (red circles) determined at different current densities from the discharge curves in c and e, respectively. The gravimetric capacity and current density values are given relative to the total mass of the $NbSe_2$-based electrode; the figures would be a factor of ~1.85 larger if given relative to the mass of active material (i.e., mass of $NbSe_2$ only). **(f)** Cyclability of $NbSe_2$ nanorolls (orange trace) and nanosheets (red trace) in terms of capacity (solid trace) and Coulombic efficiency (dotted trace) at a current density of 0.5 A g^{-1}. **(g)** Typical GCD for the early stages of cycling of the $NbSe_2$ nanorolls (green traces) and for the electrode with increased capacity after several hundred cycles (blue traces). For ease of comparison, the profiles have been normalized to their full discharge capacity.

Quantitative comparison of the CVs for the nanorolls and unfolded nanosheets revealed that consistently higher currents were measured with the former material, implying its higher electrochemical activity (the mass loading of both samples was the same, i.e., ~0.65 mg cm^{-2}). Such a result was consistent with the idea that tubular morphologies should be more conducive to facilitating access of the electrolyte to the active material, compared to the case of unfolded nanosheets [67,68]: the strong tendency of the latter to re-stack upon processing should be substantially alleviated when the nanosheets are rolled-up into nanorolls. The larger electrode-electrolyte contact area expected for the rolled-up nano-objects was reflected in the much more intense current associated to the generation of the SEI layer (i.e., the cathodic peak at

~0.15 V vs. Li/Li^+ of the first CV) in this sample relative to that of the unfolded nanosheets, as can be noticed in Fig. 4a and b. Due to the irreversible formation of the SEI layer as well as to the partial irreversibility of the intercalation and conversion events in $NbSe_2$, the Coulombic efficiency of the first voltammetric cycle was rather low, and even more so for the nanorolls (~58% vs 62% for the unfolded nanosheets), but in both cases the efficiency tended to approach 100 % upon subsequent cycles.

Typical galvanostatic charge-discharge (GCD) profiles recorded at different current densities between 0.1 and 5 A g^{-1} after the first few initial cycles are presented in Fig. 4c and d for the nanorolls and unfolded nanosheets, respectively. As expected, larger capacity values were obtained with the rolled-up nano-objects both at low and high current densities. For example, capacities of ~300 (nanorolls) and ~130 (unfolded nanosheets) mAh g^{-1} at 0.1 A g^{-1}, as well as ~130 (nanorolls) and ~60 (unfolded nanosheets) mAh g^{-1} at 5 A g^{-1} were measured. More detailed data of the rate capability of the samples are given in Fig. 4e. In both cases, about ~45% of the capacity could be retained when the current density was increased from 0.1 to 5 A g^{-1}. We note that these gravimetric capacity and current density figures are given relative to the total mass of the $NbSe_2$-based electrode. If given relative to the mass of active material (i.e., mass of $NbSe_2$ only), the capacities/current densities would be a factor of ~1.85 larger. Taking this point into account is important when making comparisons with results from the literature, where the distinction between total mass of the electrode and mass of active material in gravimetric data is not always explicitly stated. When such comparisons were possible on an equal footing, the present cathodically delaminated $NbSe_2$ material was seen to exhibit a very good performance. Specifically, the Li storage capacities for the rolled-up nano-objects were competitive with recent excellent results from a few-layer $NbSe_2$@graphene heterostructure obtained by a wet ball milling technique [15].

Relative to the mass of active material, the $NbSe_2$@graphene heterostructure yielded capacities of 492 and 416 mAh g^{-1} at 0.1 and 3 A g^{-1}, respectively, to be compared with values of 545 and 325 mAh g^{-1} at 0.18 and 3.7 A g^{-1}, respectively, measured for the present $NbSe_2$ nanoroll sample (see Table S1 in the supporting information for a comparison of the electrochemical performance of the materials prepared here with the very few examples reported in the literature for $NbSe_2$-based materials applied to Li storage).

The cyclic behavior of the delaminated $NbSe_2$ materials was also investigated, and the corresponding results (capacity and Coulombic efficiency values) are shown in Fig. 4f for tests carried out at a current density of 0.5 A g^{-1} (relative to the total mass of the electrode). Remarkably, the capacity was seen to increase to a large extent after several hundred charge-discharge cycles, especially in the case of the nanorolls (orange solid trace), e.g., it was a factor of ~3 times higher (up to 750–800 mAh g^{-1}) for this sample upon 700–800 cycles, compared to a factor of ~2 (up to 200–220 mAh g^{-1}) for the unfolded nanosheets (red solid trace). Nonetheless, after about 900 cycles, the capacity of the nanorolls plummeted to values below 50 mAh g^{-1} over the course of several tens of cycles (~0.1% of capacity decrease per cycle), which was indicative of severe cell failure. By contrast, that of the unfolded nanosheets continued to rise up to ~320 mAh g^{-1} for some additional 300 cycles, reaching a plateau subsequently and starting to decline slowly (~0.06% per cycle) after 1600 cycles (see Fig. S9). The steady increase in capacity upon repeated cycling would appear to suggest that not all of the active material in the electrode was initially available for Li storage. This could be due to the barrier effect of the binder and/or conductive additive, the contact of which with particles of the active material would hamper access of the electrolyte to the latter, thus compromising their activity [15]. The local volume changes associated to recurrent

lithiation/delithiation of the active particles would likely promote the opening of gaps between such particles and the binder/conductive additive, which in turn would facilitate a more extensive infiltration of the electrolyte. The fact that no such an improvement in rate capability was observed between nanoroll and nanosheet morphology (see Fig. 4e) must be related to the protocol used to prepare the electrodes, i. e., casting a mixture of lyophilized powder with additives onto copper foil (see Experimental Section in the Supporting Information for details), which favors re-stacking of the nanosheets, but to a limited extent. If a method more prone to re-stacking of the nanosheets, such as, e. g., filtering dispersions of the active material to yield films, had been used, the lower tendency to re-stack of the nanorolls would be expected to lead to a better performance in the rate capability tests as well.

It is worth noting, however, that the maximum capacities measured here relative to the mass of $NbSe_2$, i.e., ~1450 mAh g^{-1} for the nanorolls and ~600 mAh g^{-1} for the unfolded nanosheets, were much larger than the theoretical capacity calculated for this LTMD in bulk form, i.e., ~427 mAh g^{-1}, which was obtained assuming a full conversion to Li_2Se and Nb. This suggests that Li storage mechanisms other than those described above must contribute heavily to the measured capacities. Similar to the case of graphene with respect to graphite [69], the present large excess capacity likely arises from the formation of Li multilayers on the surface of the $NbSe_2$ nano-objects, and maybe also on the surface of the carbon particles used as a conductive additive. Such a Li storage process would be expected to occur at very low potentials (e.g., below 0.3 V vs. Li/Li^+). Indeed, a large fraction of the measured capacities was seen to come from that potential range (Fig. 4c and d). To further explore this question, Fig. 4g plots two GCD profiles from the rolled-up nano-objects, one of them typical of the early stages of cycling (cycle no. 20, green traces) and the other one typical of the electrode with

increased capacity after several hundred cycles (cycle no. 700, blue traces). An equivalent plot for the unfolded nanosheets is shown in Fig. S10. To facilitate comparisons, the profiles have been normalized to their respective capacity, that is, with the full discharge capacity equaling to 100%. If the large excess capacity built up steadily over several hundred cycles was only due to the progressive formation of Li multilayers, we would expect the corresponding discharge profile to be considerably skewed towards very low potentials compared to that obtained during the initial cycles. Nevertheless, as noticed from Fig. 4g and S8, that was not the case. Rather, the two discharge profiles were very similar to each other in the two samples. This result implied that the active material in the electrode became increasingly available as a whole upon cycling, i.e., not just the outer surface of the particles for the formation of Li multilayers, but also simultaneously the interior of the $NbSe_2$ nano-objects for intercalation/conversion reactions.

On the other hand, as also noticed in Fig. 4g and S8, the normalized charge profiles skewed towards higher potentials upon prolonged cycling, particularly in the case of the nanorolls, indicative of an increased polarization of the cell. Although the origin of this effect is currently unclear, we believe it may be related to ohmic processes (ohmic polarization) [70]. As the gaps between active $NbSe_2$ particles and binder/conductive additive progressively open, the quality of the electrical contacts between the electrode components can be expected to decrease, which would be possibly further promoted by the formation of additional SEI layers in the new gaps. This would result in an electrode with poorer electrical conductivity and, consequently, with increased polarization of ohmic nature. The increasingly poor electrical contacts within the electrode could also be responsible for the capacity decay noticed in the cells. Specifically, the larger surface area associated to the $NbSe_2$ nanoscrolls compared to the unfolded nanosheets, while

attractive for promoting higher Li storage capacities, would also be conducive to a more extensive opening of gaps. In turn, this would lead to a more drastic deterioration of the electrical contacts within the electrode and thus to a faster capacity decay in the former sample, as was actually seen in Figs. 4f and S8. The abrupt morphological changes during charge/discharge would also lead to sudden changes in the electrical contacts, yielding a zigzagging curve, as seen in the latter figures. A more in-depth investigation of the failure mechanisms of this electrode material will be provided in future work, with the aim of proposing strategies that improve its cycle life performance.

3. Conclusions

We have demonstrated a simple and expeditious method for the preparation of 2D $NbSe_2$ predominantly in the form of either rolled-up nanosheets (nanorolls) or unfolded nanosheets. This method relies on the direct cathodic exfoliation of bulk $NbSe_2$ powder in an aqueous solution of a readily available salt, which makes it especially attractive from a practical standpoint. The fact that the exfoliated nano-objects could be directly obtained by the present electrolytic treatment in a very short time (1–2 minutes) with substantial yields (~16 wt%) sets this strategy apart from most other top-down methods previously used for the production of 2D $NbSe_2$, such as direct liquid-phase exfoliation via sonication (longer processing times, lower yields) and typical electrochemical exfoliation techniques (use of organic electrolytes, post-treatment required to complete delamination). An inquiry into the cathodic exfoliation mechanism suggested that delamination is driven by a partial hydrolytic oxidation of the material in the locally alkaline environment around the $NbSe_2$ cathode. This reaction is expected to generate molecular niobium oxide species (e.g., highly charged polyoxoniobates) that prompt the cleavage of thin $NbSe_2$ layers from their bulk parent solid, in a process that resembles

the redox exfoliation mechanism of LTMDs. As expected from the particulars of the exfoliation mechanism, the methodology could be extended to other metallic LTMDs, such as NbS_2 and VSe_2. As an active material for electrochemical lithium storage, the cathodically delaminated products were seen to exhibit very high capacity values, particularly the material with dominant nanoroll morphology. This can be ascribed to a higher accessibility of the lithium storage sites afforded by such a morphology (larger electrode-electrolyte contact area) compared to the material with unfolded nanosheet morphology, where re-stacking issues probably constitute a barrier in that respect. Overall, the present results make metallic 2D LTMDs available by a simple and fast preparation strategy of low environmental impact, which is expected to expedite their uses in electrochemical energy storage and beyond.

Supporting Information: The Supporting Information is available free of charge at https://pubs.acs.org/doi/10.1021/acsaem.xxxxxxx

- Experimental section; evidence on the reversibility of the folding of the $NbSe_2$ nanosheets into nanoroll morphology through solvent exchange; further physicochemical characterization of cathodically delaminated $NbSe_2$; cathodical delamination of other LTMDs (NbS_2 and VSe_2); comparison of the electrochemical performance for Li storage of the cathodically delaminated $NbSe_2$ with other $NbSe_2$-based materials; additional information of the cyclability of the cathodically delaminated $NbSe_2$ materials for lithium storage (PDF).
- Movie 1 demonstrating the electrochemical delamination of $NbSe_2$ bulk material pressed on flexible graphite for the preparation of $NbSe_2$ nanosheets (MP4).

- Movie 2 demonstrating the change undergone by flexible graphite alone under the same conditions (MP4).
- Movie 3 demonstrating the electrochemical delamination of a pellet $NbSe_2$ bulk material (MP4).
- Movie 4 demonstrating the electrochemical delamination of NbS_2 into of NbS_2 nanosheets (MP4).
- Movie 5 demonstrating the electrochemical delamination of VSe_2 into of VSe_2 nanosheets (MP4).

Acknowledgements

D. F. C., S. G.-D, S. V.-R., J. M. M., J. I. P. gratefully acknowledge funding by the Spanish Ministerio de Ciencia e Innovación and Agencia Estatal de Investigación (MCIN/AEI/ 10.13039/501100011033) as well as the European Regional Development Fund (ERDF, A way of making Europe) through grant PID2021-125246OB-I00, and by Plan de Ciencia, Tecnología e Innovación (PCTI) 2018-2022 del Principado de Asturias and the ERDF through grant IDI/2021/000037. S.G.-D. is grateful to the Spanish MINECO for his pre-doctoral contract [BES/2016 077830]. E. R.-P. thanks the Région Centre val de Loire in France [Project APR-IR SCAP-3D, convention n°2017-00117284] for financial support.

References

[1] Novoselov, K.S.; Mishchenko, A.; Carvalho, A.; Castro Neto, A.H. 2D materials and van der Waals heterostructures, Science 353 (2016) aac9439.

[2] Kumar, K.S.; Choudhary, N.; Jung, Y.; Thomas, J. Recent advances in two-dimensional nanomaterials for supercapacitor electrode applications, ACS Energy Lett. 3 (2018) 482-495.

[3] Yuan, D.; Dou, Y.; Wu, Z.; Tian, Y.; Ye, K.-H.; Lin, Z.; Dou, S.X.; Zhang, S. Atomically thin materials for next-generation rechargeable batteries, Chem. Rev. 122 (2022) 957-999.

[4] Cui, H.; Guo, Y.; Ma, W.; Zhou, Z. 2D materials for electrochemical energy storage: design, preparation, and application, ChemSusChem 13 (2020) 1155-1171.

[5] El-Kady,M.F.; Shao, Y.; Kaner, R.B. Graphene for batteries, supercapacitors and beyond, Nat. Rev. Mater.1 (2016) 16033.

[6] Wu, J.; Ciucci, F.; Kim, J.-K. Molybdenum disulfide based nanomaterials for rechargeable batteries, Chem. Eur. J. 26 (2020) 6296-6319.

[7] Xiong, D.; Li, X.; Bai, Z.; Lu, S. Recent advances in layered $Ti_3C_2T_x$MXene for electrochemical energy storage, Small 14 (2018) 1703419.

[8] Tao, Y.; Huang, T.; Ding, C.; Yu, F.; Tan, D.; Wang, F.; Xie, Q.; Yao, S. Few-layer phosphorene: an emerging electrode material for electrochemical energy storage, Appl. Mater. Today 15 (2019) 18-33.

[9] Tan, H.T.; Sun, W.; Wang, L.; Yan, Q. 2D transition metal oxides/hydroxides for energy-storage applications, ChemNanoMat2 (2015) 562-577.

[10] Pomerantseva, E.; Bonaccorso, F.; Feng, X.; Cui, Y.; Gogotsi, Y. Energy storage: the future enabled by nanomaterials, Science 366 (2019) eaan8285.

[11] Jeong, G.H.; Sasikala, S.P.; Yun, T.; Lee, G.Y.; Lee, W.J.; Kim, S.O. Nanoscale assembly of 2D materials for energy and environmental applications, Adv. Mater. 32 (2020) 1907006.

[12] Zhao, B.; Shen, D.; Zhang, Z.; Lu, P.; Hossain, M.; Li, J.; Li, B.; Duan, X. 2D metallic transition metal dichalcogenides: structures, synthesis, properties, and applications, Adv. Funct. Mater.31 (2021) 2105132.

[13] Peng, C.; Lyu, H.; Wu, L.; Xiong, T.; Xiong, F.; Liu, Z.; An, Q.; Mai, L. Lithium- and magnesium-storage mechanisms of novel hexagonal $NbSe_2$, ACS Appl. Mater. Interfaces 10 (2018) 36988-36995.

[14] Zhang, J.; Du, C.; Zhao, J.; Ren, H.; Liang, Q.; Zheng, Y.; Madhavi, S.; Wang, X.; Zhu, J.; Yan, Q. $CoSe_2$-decorated $NbSe_2$ nanosheets fabricated via cation exchange for Li storage, ACS Appl. Mater. Interfaces 10 (2018) 37773-37778.

[15] Nguyen, Q.H.; Kim, H.; Kim, I.T.; Choi, W.; Hur, J. Few-layer $NbSe_2$@graphene heterostructures as anodes for lithium-ion half- and full-cell batteries, Chem. Eng. J. 382 (2020) 122981.

[16] Luo, Y.; Han, J.; Ma, Q.; Zhan, R.; Zhang, Y.; Xu, Q.; Xu, M. Exploration of $NbSe_2$ flakes as reversible host materials for sodium-ion and potassium-ion batteries, ChemistrySelect 3 (2018) 9807-9811.

[17] Xu, B.; Ma, X.; Tian, J.; Zhao, F.; Liu, Y.; Wang, B.; Yang, H.; Xia, Y. Layer-structured $NbSe_2$ anode material for sodium-ion and potassium-ion batteries, Ionics 25 (2019) 4171-4177.

[18] Peng, Q.; Ling, F.; Yang, H.; Duan, P.; Xu, R.; Wang, Q.; Yu, Y. Boosting potassium storage performance via construction of $NbSe_2$-based misfit layered chalcogenides, Energy Storage Mater. 39 (2021) 265-270.

[19] Park, M.J.; Asl, H.Y.; Manthiram, A. Understanding Zn-ion insertion chemistry through nonaqueous electrochemical investigation of 2H-$NbSe_2$, Adv. Mater. Interfaces 8 (2021) 2100878.

[20] Yang, D.; Liang, Z.; Zhang, C.; Biendicho, J.J.; Botifoll, M.; Spadaro, M.C.; Chen, Q.; Li, M.; Ramon, A.; Moghaddam, A.O.; Llorca, J.; Wang, J.; Morante, J.R.; Arbiol, J.; Chou, S.-L.; Cabot, A. $NbSe_2$ meets C_2N: a 2D-2D heterostructure catalysts as multifunctional polysulfide mediator in ultra-long-life lithium-sulfur batteries, Adv. Energy Mater. 11 (2021) 2101250.

[21] Sun, G.; Liu, J.; Zhang, X.; Wang, X.; Li, H.; Yu, Y.; Huang, W.; Zhang, H.; Chen, P. Fabrication of ultralong hybrid microfibers from nanosheets of reduced graphene oxide and transition-metal dichalcogenides and their application as supercapacitors, Angew. Chem. Int. Ed. 53 (2014) 12576-12580.

[22] Ahmad, H.M.N.; Ghosh, S.; Dutta, G.; Maddaus, A.G.; Tsavalas, J.G.; Hollen, S.; Song, E. Effects of impurities on the electrochemical characterization of liquid-phase exfoliated niobium diselenide nanosheets, J. Phys. Chem. C 123 (2019) 8671-8680.

[23] Coleman, J.N.; Lotya, M.; O´Neill, A.; Bergin, S.D.; King, P.J.; Khan, U.; Young, K.; Gaucher, A.; De, S.; Smith, R.J.; Shvets, I.V.; Arora, S.K.; Stanton, G.; Kim, H.-Y.;

Lee, K.; Kim, G.T.; Duesberg, G.S.; Hallam, T.; Boland, J.J.; Wang, J.J.; Donegan, J.F.; Grunlan, J.C.; Moriarty, G.; Shmeliov, A.; Nicholls, R.J.; Perkins, J.M.; Grieveson, E.M.; Theuwissen, K.; McComb, D.W.; Nellist, P.D.; Nicolosi, V. Two-dimensional nanosheets produced by liquid exfoliation of layered materials, Science 331 (2011) 568-571.

[24] Zeng, Z.; Sun, T.; Zhu, J.; Huang, X.; Yin, Z.; Lu, G.; Fan, Z.; Yan, Q.; Hng, H.H.; Zhang, H. An effective method for the fabrication of few-layer-thick inorganic nanosheets, Angew. Chem. Int. Ed. 51 (2012) 9052-9056.

[25] Lin, Z.; Liu, Y.; Halim, U.; Ding, M.; Liu, Y.; Wang, Y.; Jia, C.; Chen, P.; Duan, X.; Wang, C.; Song, F.; Li, M.; Wan, C.; Huang, Y.; Duan, X. Solution-processable 2D semiconductors for high-performance large-area electronics, Nature 562 (2018) 254-258.

[26] Li, J.; Song, P.; Zhao, J.; Vaklinova, K.; Zhao, X.; Li, Z.; Qiu, Z.; Wang, Z.; Lin, L.; Zhao, M.; Herng, T.S.; Zuo, Y.; Jonhson, W.; Yu, W.; Hai, X.; Lyu, P.; Xu, H.; Yang, H. Chen, C.; Pennycook, S.J.; Ding, J.; Teng, J.; Neto, A.H.C.; Novoselov, K.S.; Lu, J. Printable two-dimensional superconducting monolayers, Nat. Mater. 20 (2021) 181-187.

[27] García-Dalí, S.; Paredes, J.I.; Munuera, J.M.; Villar-Rodil, S.; Adawy, A.; Martínez-Alonso, A.; Tascón, J.M.D. Aqueous cathodic exfoliation strategy toward solution-processable and phase-preserved MoS_2 nanosheets for energy storage and catalytic applications, ACS Appl. Mater. Interfaces 11 (2019) 36991-37003.

[28] Calavalle, F.; Dreher, P.; Surdendran, A.P.; Wan, W.; Timpel, M.; Verucchi, R.; Rogero, C.; Bauch, T.; Lombardi, F.; Casanova, F.; Nardi, M.V.; Ugeda, M.M.; Hueso, L.E.; Gobbi, M. Tailoring superconductivity in large-area single-layer $NbSe_2$ via self-assembled molecular adlayers, Nano Lett. 21 (2021) 136-143.

[29] CRC Handbook of Chemistry and Physics, Lide, D. R. (Ed.), 87^{th} Ed. 2006, pp. 8-21 & 8-22.

[30] Chen, J.; Yang, J.; Chen, B.; Liu, S.; Dong, J.; Li, C. Large-scale synthesis of $NbSe_2$ nanosheets and their use as nanofillers for improving the tribological properties of epoxy coatings, Surf. Coat. Technol. 305 (2016) 23-28.

[31] Gates, B.; Mayers, B.; Cattle, B.; Xia, Y. Synthesis and characterization of uniform nanowires of trigonal selenium, Adv. Funct. Mater. 12 (2002) 219-227.

[32] Fresneda, M.A.R.; Martín, J.D.; Bolívar, J.G.; Cantos, M.V.F.; Bosch-Estévez, G.; Moreno, M.F.M.; Merroun, M.L. Green synthesis and biotransformation of amorphous Se nanospheres to trigonal 1D Se nanostructures: impact on Se mobility within the concept of radioactive waste disposal, Environ. Sci.: Nano 5 (2018) 2103-2116.

[33] Wang, C.S.; Chen, J.M. Raman spectrum of metallic layered compound $NbSe_2$, Solid State Commun. 14 (1974) 1145-1148.

[34] Pereira, C.M.; Liang, W.Y. Raman studies of the normal phase of 2H-$NbSe_2$, J. Phys. C: Solid State Phys. 15 (1982) L991-L995.

[35] Tsang, J.C.; Smith, J.E.; Shafer, M.W. Raman spectroscopy of soft modes at the charge-density-wave phase transition in 2H-$NbSe_2$, Phys. Rev. Lett. 37 (1976) 1407-1410.

[36] Tsang, J.C.; Smith, J.E.; Shafer, M.W. Effect of charge density wave fluctuations on the frequencies of optic phonons in 2H-$TaSe_2$ and –$NbSe_2$, Solid State Commun. 27 (1978) 145-149.

[37] Staley, N.E.; Wu, J.; Eklund, P.; Liu, Y.; Li, L.; Xu, Z. Electric field effect on superconductivity in atomically thin flakes of $NbSe_2$, Phys. Rev. B 80 (2009) 184505.

[38] Hill, H.M.; Rigosi, A.F.; Krylyuk, S.; Tian, J.; Nguyen, N.V.; Davydov, A.V.; Newell, D.B.; Walker, A.R.H. Comprehensive optical characterization of atomically thin $NbSe_2$, Phys. Rev. B 98 (2018) 165109.

[39] Vacquier, G.; Casalot, A.; Rolland, A. Superficial characterization of $NbSe_2$ single crystals: an Auger electron spectroscopy study, Mater.Sci. Eng. 85 (1987) L9-L12.

[40] Naik, S.; Kalaiarasan, S.; Nath, R.C.; Sarangi, S.N.; Sahu, A.K.; Samal, D.; Biswal, H.S.; Samal, S.L. Nominal effect of Mg intercalation on the superconducting properties of 2H-$NbSe_2$, Inorg. Chem. 60 (2021) 4588-4598.

[41] Myers, G.E.; Montet, G.L. Light-induced oxidation of $NbSe_2$ single crystals, J. Phys. Chem. Solids 32 (1971) 2645-2646.

[42] Kim, Y.; Huang, J.-L.; Lieber, C.M. Characterization of nanometer scale wear and oxidation of transition metal dichalcogenide lubricants by atomic force microscopy, Appl. Phys. Lett. 59 (1991) 3404-3406.

[43] Nguyen, L.; Komsa, H.-P.; Khestanova, E.; Kashtiban, R.J.; Peters, J.J.P.; Lawlor, S.; Sanchez, A.M.; Sloan, J.; Gorbachev, R.V.; Grigorieva, I.V.; Krasheninnikov, A.V.;

Haigh, S.J. Atomic defects and doping of monolayer $NbSe_2$, ACS Nano 11 (2017) 2894-2904.

[44] Ahmad, H.M.N.; Ghosh, S.; Dutta, G.; Maddaus, A.G.; Tsavalas, J.G.; Hollen, S.; Song, E. Effects of impurities on the electrochemical characterization of liquid-phase exfoliated niobium diselenide nanosheets, J. Phys. Chem. C 123 (2019) 8671-8680.

[45] Huang, B.X.; Wang, K.; Church, J.S.; Li, Y.-S. Characterization of oxides on niobium by Raman and infrared spectroscopy, Electrochim. Acta 44 (1999) 2571-2577.

[46] Raevskaya, A.E.; Stroyuk, A.L.; Kuchmiy, S.Y.; Dzhagan, V.M.; Zahn, D.R.T.; Schulze, S. Annealing-induced structural transformation of gelatin-capped Se nanoparticles, Solid State Commun. 145 (2008) 288-292.

[47] Tzeng, W.-Y.; Tseng, Y.-H.; Yeh, T.-T.; Tu, C.-M.; Sankar, R.; Chen, Y.-H.; Huang, B.-H.; Chou, F.-C.; Luo, C.-W. Selenium nanoparticle prepared by femtosecond laser-induced plasma shock wave, Opt. Express 28 (2020) 685-694.

[48] El-Bana, M.S.; Wolverson, D.; Russo, S.; Balakrishnan, G.; Paul, D.M.; Bending, S.J. Superconductivity in two-dimensional $NbSe_2$ field effect transistors, Supercond. Sci. Technol. 26 (2013) 125020.

[49] Kim, J.E.; Vu, V.T.; Vu, T.T.H.; Phan, T.L.; Kim, Y.R.; Kang, W.T.; Kim, K.; Lee, Y.H.; Yu, W.J. A non-volatile memory based on $NbO_x/NbSe_2$ van der Waals heterostructures, Appl. Sci. 10 (2020) 7598.

[50] Wang, B.; Luo, H.; Wang, X.; Wang, E.; Sun, Y.; Tsai, Y.-C.; Zhu, H.; Liu, P.; Jiang, K.; Liu, K. Bifunctional NbS_2-based asymmetric heterostructure for lateral and vertical electronic devices, ACS Nano 14 (2020) 175-184.

[51] Surface Analysis –The Principal Techniques. Vickerman, J. C.; Gilmore, I. S. Ch. 3: Electron Spectroscopy for Chemical Analysis, B: Ratner, D.; Castner, D. G. p.89, 2nd Ed. 2009, John Wiley & Sons.

[52] Ambrosi, A.; Pumera, M. Exfoliation of layered materials using electrochemistry, Chem. Soc. Rev. 47 (2018) 7213-7224.

[53] Fang, Y.; Li, X.; Li, J.; Yao, C.; Hoh, H.Y.; Hai, X.; Lu, J.; Su, C. Janus electrochemical exfoliation of two-dimensional materials, J. Mater. Chem. A 7 (2019) 25691-25711.

[54] Jawaid, A.; Che, J.; Drummy, L.F.; Bultman, J.; Waite, A.; Hsiao, M.-S.; Vaia, R.A. Redox exfoliation of layered transition metal dichalcogenides, ACS Nano 11 (2017) 635-646.

[55] Jawaid, A.M.; Ritter, A.J.; Vaia, R.A. Mechanism for redox exfoliation of layered transition metal dichalcogenides, Chem. Mater. 32 (2020) 6550-6565.

[56] Nyman, M. Polyoxoniobate chemistry in the 21st century, Dalton Trans. 40 (2011) 8049-8058.

[57] Ibrahem, M.A.; Huang, W.-C.; Lan, T.; Boopathi, K.M.; Hsiao, Y.-C.; Chen, C.-H.; Budiawan, W.; Chen, Y.-Y.; Chang, C.-S.; Li, L.-J.; Tsai, C.-H.; Chu, C.W. Controlled mechanical cleavage of bulk niobium diselenide to nanoscaled sheet, rod, and particle structures for Pt-free dye-sensitized solar cells, J. Mater. Chem. A 2 (2014) 11382-11390.

[58] Qu, R.; Wen, X.; Zhao, Y.; Wang, T.; Yao, R.; Lu, J. Ultrasonic-assisted top-down preparation of $NbSe_2$ micro/nanoparticles and hybrid material as solid lubricant for sliding electrical contact, Ultrason. Sonochem.73 (2021) 105491.

[59] Meng, J.; Wang, G.; Li, X.; Lu, X.; Zhang, J.; Yu, H.; Chen, W.; Du, L.; Liao, M.; Zhao, J.; Chen, P.; Zhu, J.; Bai, X.; Shi, D.; Zhang, G. Rolling up a monolayer MoS_2 sheet, Small 12 (2016) 3770-3774.

[60] Cui, X.; Kong, Z.; Gao, E.; Huang, D.; Hao, Y.; Shen, H.; Di, C.; Xu, Z.; Zheng, J.; Zhu, D. Rolling up transition metal dichalcogenide nanoscrolls via one drop of ethanol, Nat. Commun. 9 (2018) 1301.

[61] Wang, W.; Gai, Y.; Xiao, D.; Zhao, Y. A facile and general approach for production of nanoscrolls with high-yield from two-dimensional nanosheets, Sci. Rep. 8 (2018) 15262.

[62] Hwang, D.Y.; Choi, K.H.; Suh, D.H. A vacancy-driven phase transition in MoX_2 (X: S, Se and Te) nanoscrolls, Nanoscale 10 (2018) 7918-7926.

[63] Thangasamy, P.; Sathish, M. Rapid, one-pot synthesis of luminescent MoS_2 nanoscrolls using supercritical fluid processing, J. Mater. Chem. C 4 (2016) 1165-1169.

[64] Alharbi, T.M.D.; Elmas, S.; Alotabi, A.S.; Andersson, M.R.; Raston, C.L. Continuous flow fabrication of MoS_2 scrolls for electrocatalytic hydrogen evolution, ACS Sustainable Chem. Eng. 10 (2022) 9325-9333.

[65] Guillemeney, L.; Lermusiaux, L.; Landaburu, G.; Wagnon, B.; Abécassis, B. Curvature and self-assembly of semi-conducting nanoplatelets, Commun.Chem. 5 (2022) 7.

[66] Li, Q.; Zhou, Q.; Shi, L.; Chen, Q.; Wang, J. Recent advances in oxidation and degradation mechanisms of ultrathin 2D materials under ambient conditions and their passivation strategies, J. Mater. Chem. A 7 (2019) 4291-4312.

[67] Lian, Y.; Yang, N.; Wang, D.; Zheng, Y.; Ban, C.; Zhao, J.; Zhang, H. Optimization design and application of niobium-based materials in electrochemical energy storage, Adv. Energy Sustainability Res. 1 (2020) 2000038.

[68] Zou, Z.; Wang, Q.; Zhu, K.; Ye, K.; Wang, G.; Cao, D.; Yan, J. Ultrathin-walled Bi_2S_3nanoroll/MXene composite toward high capacity and fast lithium storage, Small 18 (2022) 2106673.

[69] Sonia, F.J.; Jangid, M.K.; Ananthoju, B.; Aslam, M.; Johari, P.; Mukhopadhyay, A. Understanding the Li-storage in few layers graphene with respect to bulk graphite: experimental, analytical and computational study, J. Mater. Chem. A 5 (2017) 8662-8679.

[70] Zheng, J.; Lu, J.; Amine, K.; Pan, F. Depolarization effect to enhance the performance of lithium ions batteries, Nano Energy 33 (2017) 497-507.

For Table of Contents Only